

Fermi-arcs mediated transport in surface Josephson junctions of Weyl semimetal

Rekha Kumari,^{1,*} Dibya Kanti Mukherjee,² and Arijit Kundu^{1,†}

¹*Department of Physics, Indian Institute of Technology Kanpur, Kanpur 208016, India*

²*Department of Physics, Indiana University, Bloomington, Indiana 47405, USA*

This study presents Fermi-arcs mediated transport in a Weyl semimetal thin slab, interfacing two *s*-wave superconductors. We present detailed study with both time-reversal and inversion symmetry broken Weyl semimetals under grounding, orbital magnetic fields, and Zeeman fields. An orbital magnetic field induces energy level oscillations, while a Zeeman field give rise to the periodic anomalous oscillations in the Josephson current. These anomalous oscillations correlate with the separation of Weyl nodes in momentum space, junction length, and system symmetries. Additionally, we present an explanation by scattering theory modeling the Fermi-arcs as a network model.

INTRODUCTION

Weyl semimetals (WSMs) are three-dimensional topological systems with accidental bulk degeneracies (Weyl points), near which electrons follow Weyl equations [1–7]. These Weyl points act as monopoles of the Berry curvature in momentum space with a fixed ‘chirality’ (a quantum characteristic determined by the Berry flux enclosed by a closed surface surrounding the node). These Weyl points always occur in pairs due to a no-go theorem [8, 9]. The realization of a WSM-phase requires either the breaking of time-reversal symmetry (TRS) or inversion symmetry (IR). When TRS and IR coexist, a pair of degenerate Weyl points may emerge [10–12].

Surface states of Weyl semimetals, often called *Fermi arc* states, arise due to the topological nature of the underlying bands [13–15]. These Fermi arcs connect the pairs of Weyl nodes of opposite *chirality*. The requirement that Fermi arcs connect Weyl Fermions of opposite chirality, also leads to them being (pseudo-)spin polarized [16, 17]. In a time-reversal broken (inversion broken) minimal Weyl system, an odd (even) number of such Fermi arcs would be present in the surface Brillouin zone. Being quasi-1D in nature, Fermi arcs are naturally excellent candidates for correlation physics [12, 18–22], although the presence of bulk states cannot be disregarded in describing their properties.

The chiral nature of Weyl nodes gives rise to unique bulk transport properties in Weyl semimetals [23–25]. The separation of Weyl points with opposite chirality enables charge transfer between them when subjected to parallel electric and magnetic fields, a phenomenon known as chiral anomaly. In WSMs, the charge density at an individual Weyl point is not conserved; the application of parallel *E* and *B* fields induces the movement of charges from one Weyl point to its counterpart with opposite chirality [26, 27]. This charge pumping effect induces a chemical potential difference between the paired Weyl points, termed as chiral charge imbalance

or chirality imbalance. Furthermore, at the interface of a superconductor (SC), the transport properties of Weyl electrons have been also investigated. It has been argued that, although in some cases the Andreev reflection process can be blocked [28], considering all allowed cases reveals the underlying nature of Weyl systems through Andreev reflection in an SC-Weyl-SC junction, oscillations of the Josephson current carry signatures of momentum-separated Weyl nodes [29–35].

In the case of a slab-geometry Weyl semimetal, when the Fermi energy is near the neutrality point, the Fermi surface consists of these surface states (with a higher density on one surface or another), as well as small bulk Fermi surfaces [16, 17, 36]. These surface states are characterized by a non-vanishing Chern number when projected onto a two-dimensional Brillouin zone. This zone is perpendicular to the momentum that connects pairs of Weyl points. The Josephson transport properties of these helical surface states may give rise to unique transport signatures.

This work focuses on surface Josephson transport in Weyl semimetal slabs, considering two distinct electronic configurations: one with time-reversal symmetry breaking, characterized by 2-node and one Fermi arc features, and the other with inversion symmetry breaking, characterized by 4-node and two Fermi arcs [37, 38]. In high surface-to-bulk ratio WSM geometries, Fermi-arc electrons serve as the primary Josephson current carriers, while bulk states, residing at higher energy levels, have negligible transport contributions. We investigate the Josephson current-phase relationship (CPR) using tight-binding simulations and a network model. To explore the distinct signatures associated with Fermi-arc-mediated transport, we have considered the grounded and not-grounded cases. Furthermore, we study the impact of orbital and Zeeman magnetic fields on the surface transport, which significantly affect Fermi arc length and Weyl node positions within the semimetal slabs.

This paper is structured as follows: In Sec. I, we present the electronic band structure and characteristics of Fermi arcs in both 2-node and 4-node Weyl Semimetals. This section also provides details of system setups, along with the effects of applied orbital and Zeeman magnetic fields on the positioning of Weyl nodes and the

* rekha@iitk.ac.in

† kundua@iitk.ac.in

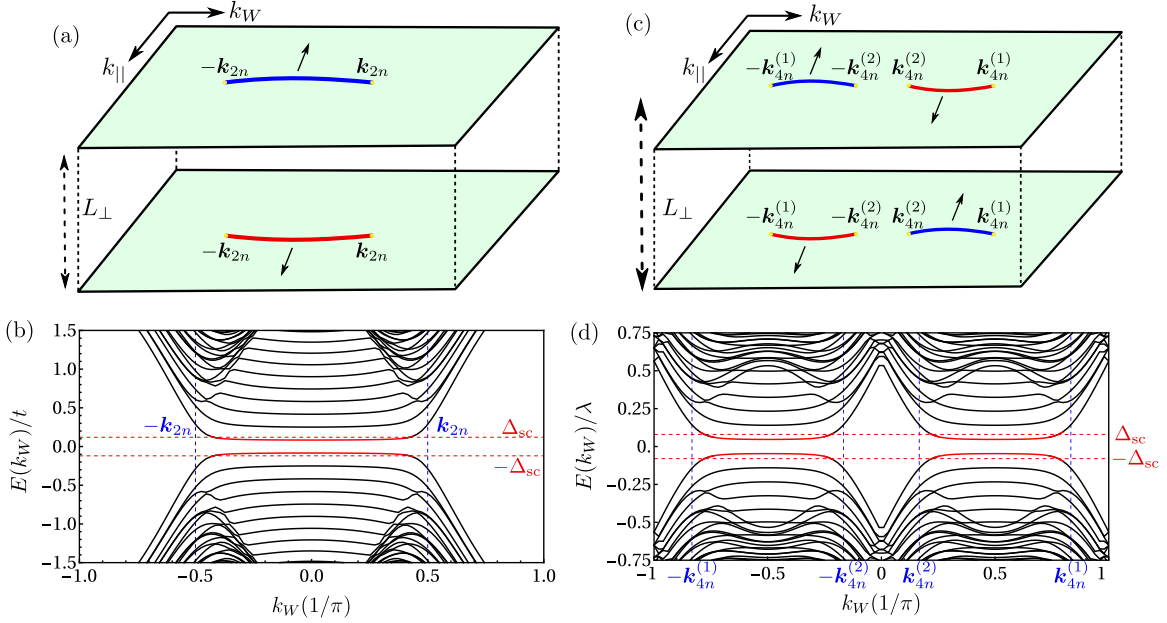


FIG. 1. Top: Schematic representations of chiral Fermi arcs in momentum space for the (a) 2-node and (c) 4-node WSMs described by Eq. (1) and Eq. (2), respectively. Bottom: The band structure of WSM slab as a function of lattice momentum k_W , the Weyl nodes (shown by vertical gridlines) in the bulk are connected by edge states, for both the (b) 2-node and (d) 4-node cases. The parameters are set as follows : $N_{\parallel} = 18, N_{\perp} = 18, m_{2n} = 2.0, t_x = 1, t = 1, k_0 = \pi/2, m_{4n} = 0.5,$ and $\lambda = 1$. The red-marked edge states denote confined states within the superconducting gap ($\pm\Delta_{sc}$), as indicated by horizontal grid-lines. This corresponds to the case of later Josephson transport, where WSM slabs are connected to superconducting reservoirs to form the Josephson junction.

length of Fermi arcs. In Sec. II, we analyze numerical and analytical results of the surface Josephson currents under various scenarios mentioned in Sec. I. Subsequently, in Section III, we have presented the significance of our work, along with its broader implications, and conclusions drawn from this study. In the Appendix, Sec. A and Sec. B outline the tight-binding Hamiltonian for the system along with the computational details of current using the non-equilibrium Green's function formalism and the symmetries of the system, respectively.

I. SYSTEM SETUP

Electronic configurations

We study two lattice models of WSMs that involve breaking of time reversal and inversion symmetries. Minimal models of them are characterized by the presence of one (two) Fermi arcs and two (four) weyl-nodes in the bulk spectrum, respectively.

The first one is a 2-band model [37] that describes electrons in a simple cubic lattice, given by the Hamiltonian

$$H_{2n} = m_{2n}(2 - \cos k_{\parallel} - \cos k_{\perp})\sigma_x + 2t_x(\cos k_W - \cos k_0)\sigma_x + 2t \sin k_{\parallel}\sigma_y + 2t \sin k_{\perp}\sigma_z. \quad (1)$$

Here, σ_i represents Pauli spin matrices, and the Weyl nodes are located at $\pm\mathbf{k}_{2n} = (k_{\parallel}, k_W, k_{\perp}) = (0, \pm k_0, 0)$

with $t_x = t, m_{2n} = 2t$. All momentum here are made unitless by scaling with inverse lattice-spacing (a_0). The time-reversal symmetry (given by $\mathcal{T}_{2n} = i\sigma_y\mathcal{K}|_{\vec{k} \rightarrow -\vec{k}}$, \mathcal{K} being complex conjugation) is broken, while inversion symmetry ($\mathcal{P}_{2n} = \sigma_x$) is preserved. Throughout the text, we set $\hbar = 1$.

The second model is a 4-band model [38] that describes electrons in a simple cubic lattice with two orbitals per site. The corresponding Hamiltonian is given by:

$$H_{4n} = \lambda s_0(\sigma_x \sin k_{\parallel} + \sigma_y \sin k_W + \sigma_z \sin k_{\perp}) + t s_y \sigma_y (2 + m_{4n} - \cos k_{\parallel} - \cos k_{\perp}). \quad (2)$$

Here, s_i and σ_i represent the Pauli matrices associated with orbital and spin degrees of freedom, respectively. The parameter λ represents the strength of the spin-orbital coupling term and we have set t to 1. When $m_{4n} > \lambda$ (taking $\lambda > 0$), the Hamiltonian corresponds to a trivial insulating phase. For $m_{4n} = \lambda$, the model Hamiltonian exhibits two Dirac nodes located at $(k_{\parallel}, k_W, k_{\perp}) = (0, \pm\pi/2, 0)$. For $|m_{4n}| < \lambda$, the Hamiltonian corresponds to a Weyl semimetal phase. In this case, each Dirac node splits into two Weyl nodes, situated at $\pm\mathbf{k}_{4n}^{(1)} = \{0, \pi - \sin^{-1}(|m_{4n}/\lambda|), 0\}, \pm\mathbf{k}_{4n}^{(2)} = \{0, \pm \sin^{-1}(|m_{4n}/\lambda|), 0\}$. In this 4-node case, time-reversal symmetry is preserved, while inversion symmetry is broken. The inversion and time-reversal symmetry operators are denoted by $\mathcal{P}_{4n} = s_x\sigma_x$ and $\mathcal{T}_{4n} = i s_0\sigma_y\mathcal{K}|_{\vec{k} \rightarrow -\vec{k}}$, respectively.

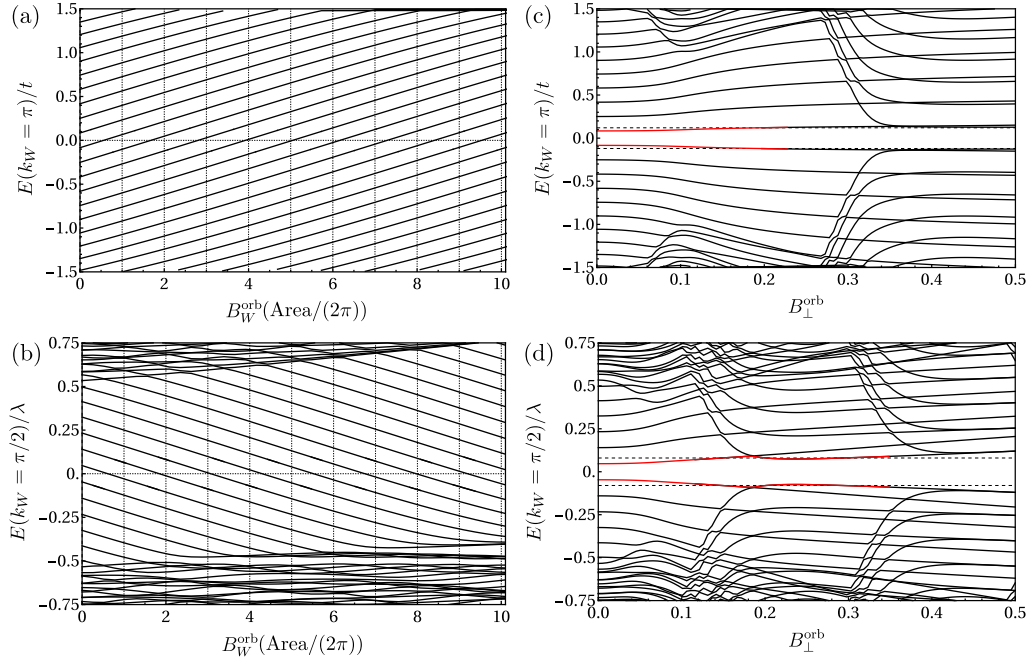


FIG. 2. Top: The energy spectrum dependence is shown for the orbital field along x_W (in units of ‘Area/ 2π ’) in (a) and (b) for the 2-node and 4-node cases, respectively. ‘Area’ is the area of the WSM slab given by $(L_{\parallel} - 1)(L_{\perp} - 1)a_0^2$. The energy spectrum dependence is shown for the orbital field along x_{\perp} in (c) and (d) for the 2-node and 4-node cases, respectively. Parameters are the same as in Fig. 1.

We consider our system (described either by Eq. 1 or Eq. 2) with finite dimensions along x_{\parallel} (longitudinal) and x_{\perp} (transverse) directions. The dimensions of this WSM slab are $L_{\parallel} = (N_{\parallel} - 1)a_0$ and $L_{\perp} = (N_{\perp} - 1)a_0$ for length and width, where N_{\parallel} and N_{\perp} represent lattice sites along their respective directions, and a_0 is the lattice spacing. For the rest of the text, we set $a_0 = 1$, such that our lengths are scaled by the lattice spacing.

For the 2-node WSM, a single Fermi arc is present on the surface Brillouin zone, as shown schematically in the Fig. 1(a). The corresponding energy spectrum of the WSM slab is depicted in Fig. 1(b) where the presence of these helical surface states are visible. In the case of the 4-node WSM, two chiral Fermi arcs are present, as shown in Fig. 1(c). This leads to the emergence of two types of helical surface states and the corresponding energy spectrum of the WSM slab is illustrated in Fig. 1(d).

Effect of Orbital Magnetic Fields: An orbital magnetic field is introduced by $\vec{k} \rightarrow \vec{k} - e\vec{A}^{\text{orb}}$, where \vec{A}^{orb} represents the vector potential associated with the orbital magnetic field. In a slab geometry, when an orbital magnetic field is applied in the x_W direction and is given by the vector potential $\vec{A}_W^{\text{orb}} = B_W^{\text{orb}}x_{\perp}\hat{x}_{\parallel}$, a repeating structure in energies appears, as shown in Fig. 2(a) and Fig. 2(b) for the 2-node and 4-node WSMs, respectively. The oscillation period (of B_W^{orb}) of this recurring energy structure is given by $\frac{2\pi}{\text{Area}}$, here, ‘Area’ represents the surface area of the slab, expressed as $(L_{\parallel} - 1)(L_{\perp} - 1)a_0^2$ and n is an integer. For each value of n , there exists a crossing of an energy level with the Fermi level.

Furthermore, when an orbital magnetic field is applied in the x_{\perp} direction and is given by the vector potential $\vec{A}_{\perp}^{\text{orb}} = B_{\perp}^{\text{orb}}x_{\parallel}\hat{x}_W$, it results in a shift of the energy lev-

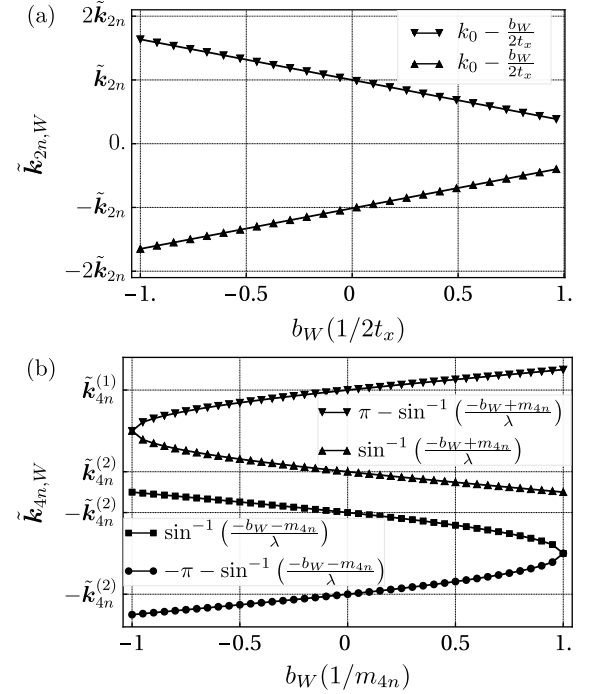


FIG. 3. Shift in the positions of Weyl node along the k_W axis with respect to b_W Zeeman field for (a) 2-node and (b) 4-node WSMs.

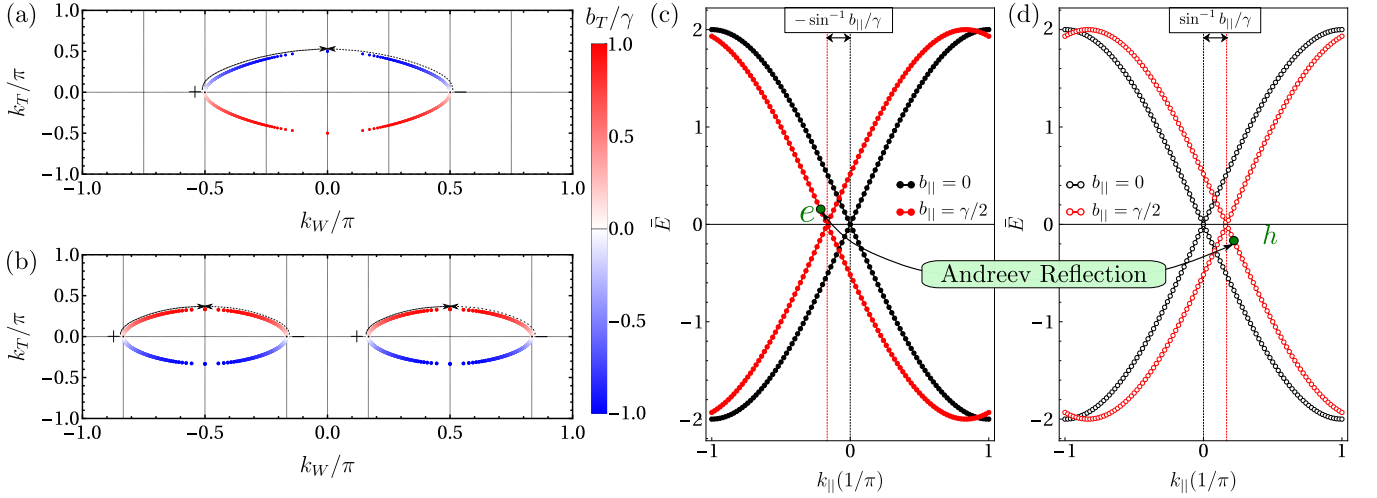


FIG. 4. Zeeman field-induced displacement of Weyl nodes in 2-node and 4-node WSMs (indicated by arrows). Shifted positions of Weyl nodes in the (k_W, k_T) plane in presence applied Zeeman field B_T , shown for the (a) 2-node and (b) 4-node WSMs, respectively. The colorbar indicates the strength of the Zeeman field. The Zeeman field b_{\parallel} induces opposing shifts in (c) electronic and (c-d) hole bands. The Andreev-reflection processes, shown in (c-d), lead to formation of Andreev bound states from the Fermi arcs. There can be two possible kinds, One Fermi Arc Andreev (OFAR) processes, when these are within the states of the same Fermi arc, and Two Fermi Arc Andreev (tFAR) processes, when these are within the states of two different Fermi arcs. In the case of 2-node WSMs, $\gamma = 2t_x$, $\bar{E} = E/t$, with k_W given by $\tilde{\mathbf{k}}_{2n,W}$ in (c) and $-\tilde{\mathbf{k}}_{2n,W}$ in (d). For 4-node WSMs, $\gamma = \sqrt{(1 - m_{4n}^2)}$, $\bar{E} = E/\lambda$, with k_W given by $\tilde{\mathbf{k}}_{4n,W}^{(1)}$ in (c) and $-\tilde{\mathbf{k}}_{4n,W}^{(1)}$ in (d).

els of the surface states, as illustrated in Fig. 2(c) and Fig. 2(d) for the 2-node and 4-node Weyl semimetals, respectively.

Effect of Zeeman Fields: To account for the influence of a Zeeman field, the Hamiltonians for the 2-node (given in Eq. (1)) and 4-node (given in Eq. (2)) incorporate the following terms, respectively:

$$H_B^{2n} = b_W \sigma_x + b_{\parallel} \sigma_y + b_{\perp} \sigma_z \quad (3)$$

$$H_B^{4n} = b_{\parallel} \sigma_x + b_W \sigma_y + b_{\perp} \sigma_z. \quad (4)$$

In presence of these additional Zeeman field terms in the Hamiltonian the modified position of the Weyl nodes in the case of 2-node and 4-node WSM are given by:

$$\tilde{\mathbf{k}}_{2n} = (\sin^{-1} \alpha_{\parallel}, \pm f_{\alpha_{\parallel}, \alpha_W, \alpha_{\perp}}, \sin^{-1} \alpha_{\perp}); \quad (5)$$

$$\tilde{\mathbf{k}}_{4n} = (\sin^{-1} \beta_{\parallel}, \{\sin^{-1} (\pm g_{\beta_{\parallel}, \beta_W, \beta_{\perp}}), \pm \pi - \sin^{-1} (\pm g_{\beta_{\parallel}, \beta_W, \beta_{\perp}})\}, \sin^{-1} \beta_{\perp}); \quad (6)$$

respectively. Here, in the above equations:

$$f_{\alpha_{\parallel}, \alpha_{\perp}} = k_0 - \alpha_W - \bar{m}_{2n} (2 - (1 - \alpha_{\parallel}^2)^{1/2} - (1 - \alpha_{\perp}^2)^{1/2}),$$

$$g_{\beta_{\parallel}, \beta_{\perp}} = \bar{m}_{4n} - \beta_W + 2 - (1 - \beta_{\parallel}^2)^{1/2} - (1 - \beta_{\perp}^2)^{1/2}.$$

$$\alpha_{\parallel(\perp)} = b_{\parallel(\perp)}/2t, \quad \beta_{\parallel(\perp)} = b_{\parallel(\perp)}/\lambda, \quad \alpha_W = b_W/2t_x, \quad \beta_W = b_W/\lambda, \quad \bar{m}_{2n} = m_{2n}/2t_x, \quad \text{and} \quad \bar{m}_{4n} = m_{4n}/\lambda.$$

In Fig. 3(a) and Fig. 3(b), the variation in the length of Fermi arc(s) is presented as a function of b_W for the 2-node and 4-node cases, respectively. In the 2-node case, it is observed that the Zeeman field changes the length

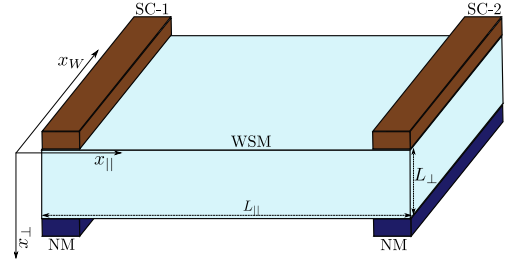


FIG. 5. System setup: s-wave superconducting leads, spaced L_{\parallel} apart, attach to WSM's top surface. The bottom surface connected to normal leads and the top and bottom surfaces spaced L_{\perp} apart.

of the Fermi arc. In contrast, within the 4-node case, the Zeeman field term induces relative difference in the lengths of Fermi arcs.

In Fig. 4(a) and Fig. 4(b), we illustrate the displacement of the Weyl node in the (k_W, k_T) plane as a function of the Zeeman field b_T for the 2-node and 4-node cases, respectively. The colorbar denotes the magnitude of the Zeeman field. We observe that as the Zeeman field b_T increases, the separation of Weyl nodes along the k_W direction decreases, consequently leading to a reduction in the length of the Fermi arc. Specifically, for $b_T = \gamma$, we observe the annihilation of Weyl nodes with opposite chirality, as depicted by arrows in Fig. 4(a-b). The reduction in the length of the Fermi arcs results in a decrease in the number of surface states participating in Josephson transport. Additionally, b_T induces shifts in the locations of Weyl nodes along the k_T direction.

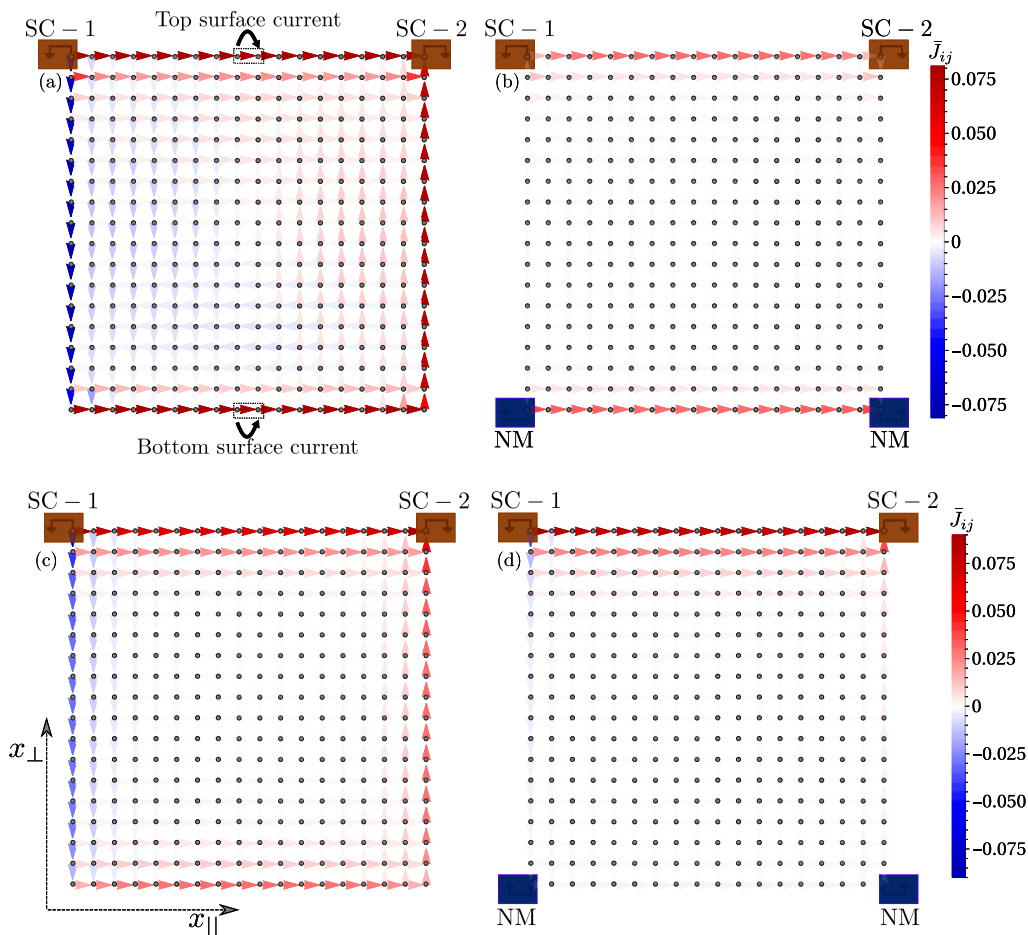


FIG. 6. The bond current distribution on the square lattice of the 2-node WSM is depicted. Panels (a) and (b) depict the difference $J_{ij}(\delta\phi = \pi/2) - J_{ij}(\delta\phi = 0)$ in the 2-node case. Panels (c) and (d) depict the $J_{ij}(\delta\phi = \pi/2)$ in the 4-node case. Panels (a), (c), and (b),(d) correspond to the grounded and non-grounded scenarios, respectively. Colors define the magnitude of the Josephson current, visualized through the color bar. The parameters used are: $t_{sc} = 1$, $\mu_{sc} = 0$, $\Delta_{sc}^{2n} = 0.125$, $\Delta_{sc}^{4n} = 0.1$, $t_\lambda = 1$ and other parameters are same as given in Fig. 1.

Fig. 4(c-d) presents the shift in energy dispersion near Weyl nodes as a function of lattice momentum k_{\parallel} , for different values of the Zeeman field b_{\parallel} . In the 2-node WSM, Fig. 4(c) and Fig. 4(d) illustrate the shift in the electronic and hole bands near Weyl nodes $\mathbf{k}_{2n,W}$ and $-\mathbf{k}_{2n,W}$, as only a single Fermi arc is present. In the 4-node case, (c) and (d) show the shift in the electronic and hole bands near Weyl nodes of the first Fermi arc $\mathbf{k}_{4n,W}^{(1)}$ and $-\mathbf{k}_{4n,W}^{(1)}$, in addition to this the hole bands near the Weyl node $-\mathbf{k}_{4n,W}^{(2)}$ from the second Fermi arc accumulate the same shift as shown in (d).

When the WSM slabs are connected with the superconducting reservoirs, these low energy states contributes in the transport through Andreev reflections. In the case of 2-node WSM, in the presence of superconducting reservoirs, a top-edge electron with spin-up (spin-down) undergoes Andreev reflection as a hole state with spin-down (spin-up) along the bottom edge. This process, termed the ‘‘One Fermi Arc Andreev Reflection (OFAR) Process,’’ involves the transfer of a charge of $2e$ from left to

right reservoirs. However, when the system is grounded, the introduction of normal reservoirs induces decoherence, significantly reducing the total current.

In the case of 4-node WSM, in addition to the ‘OFAR-Process,’ another Andreev reflection process, termed the ‘Two Fermi Arc Andreev Reflection (TFAR) Process,’ occurs due to the presence of the second Fermi arc. In the TFAR process, a spin-up (spin-down) electron on the top edge reflects as a spin-down (spin-up) hole on the same edge, incorporating two Fermi arcs and one surface. This process involves both Fermi arcs and the top edge.

Setup details

To study surface transport in Weyl semimetals, we have considered two geometrical setups. The first case is the ‘not-grounded’ configuration, where at the top surface ($j = N_{\perp}$) of the WSM slab two superconducting reservoirs are connected, while the bottom surface is not

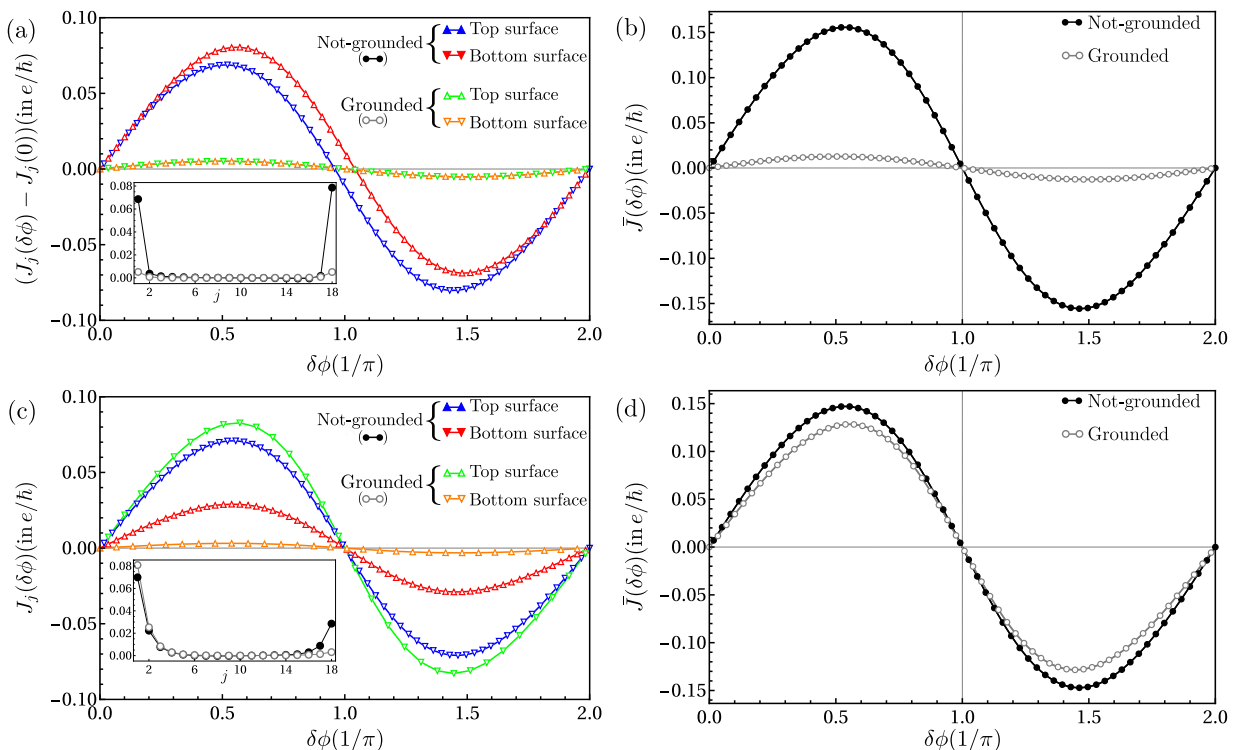


FIG. 7. Current-Phase Relations (CPR) :For the 2-node case, (a) and (b) show surface and summed Josephson currents as functions of superconducting phase difference $\delta\phi$ for both not grounded and grounded cases. Similarly, in the 4-node case, (c) and (d) show surface and summed Josephson currents as functions of superconducting phase difference $\delta\phi$ for not grounded and grounded scenarios. Insets provide the current contributions from different layers along x_{\perp} direction for each case. These currents are computed using Eq. (A9), Eq. (A10), Eq. (A11) and Eq. (A12).

connected to any reservoirs.

The second case is the ‘grounded’ configuration, where, in addition to the two superconducting reservoirs connected at the top surface, the bottom surface ($j = 1$) is connected to normal reservoirs, as illustrated in Fig. 5.

To explore transport properties of edge states, we adjust the superconducting gaps to selectively confine the minimum-energy surface states, as shown in Fig. 1 (highlighted in red). Subsequent sections elaborate on the specifics of the tight-binding Hamiltonians governing the superconducting and normal reservoirs, as well as the Weyl semimetal slabs. Moreover, the methodology encompasses a comprehensive description of the bond and net Josephson current computations employing non-equilibrium Green’s function (NEGF) techniques.

II. NUMERICAL RESULTS:

Surface Josephson effect:

The bond current distribution in the case of 2-node and 4-node WSM are shown in Fig. 6. We have computed these bond currents using the Non-Equilibrium Green’s Function (NEGF) formalism mentioned in Sec. A.

For the 2-node case, as time-reversal symmetry is al-

ready broken, a persistent surface current is there in the absence of a superconducting phase difference. The bond currents between the sites $\{(i, j) \rightarrow (i + 1, j)\}$ and $\{(i, j) \rightarrow (i, j + 1)\}$ can be computed as

$$J_{(i,j) \rightarrow (i+1,j)} = -\frac{2e}{\hbar} \text{Im} \left[\sum_{\eta\eta'} t_{ij\eta, i+1j\eta'} \langle c_{i,j,\eta}^{\dagger} c_{i+1,j,\eta'} \rangle \right], \quad (7)$$

$$J_{(i,j) \rightarrow (i,j+1)} = -\frac{2e}{\hbar} \text{Im} \left[\sum_{\eta\eta'} t_{ij\eta, ij+1\eta'} \langle c_{i,j,\eta}^{\dagger} c_{i,j+1,\eta'} \rangle \right], \quad (8)$$

respectively. Here, $t_{ij\eta, i+1j\eta'}$ incorporates the details of the hopping elements between sites (i, j) and $(i + 1, j)$ and η, η' incorporates the onsite degree of freedom indices. $\langle \dots \rangle$ is the thermal average taken over the reservoir’s states. Using this description we have computed the bond current between for sites $\{(N_{\parallel}/2, N_{\perp}) \rightarrow (N_{\parallel}/2 + 1, N_{\perp})\}$ and $\{(N_{\parallel}/2, 1) \rightarrow (N_{\parallel}/2 + 1, 1)\}$ are termed as top and bottom surface(layer) currents, respectively, as shown by arrows in Fig. 6(a).

Additionally, Fig. 6(a) and Fig. 6(b) show the distribution of bond currents on this 2D square lattice for the phase $\delta\phi = \pi/2$, obtained by subtracting the persistent currents for the not-grounded and grounded cases, respectively. For a fixed $k_W \in (-k_0, k_0)$, each edge ex-

clusively accommodates a distinct type of helical surface state. We observe that the prominent current flow occurs along the top (bottom) edges of the system, and there is a suppression in bond currents for the grounded scenario as a result of dephasing induced by normal reservoirs. The color of the colorbar represents the amplitude of the bond currents.

For the 4-node case, Fig. 6(c) and 6(d) illustrate the bond current distribution on the square lattice in the non-grounded and grounded cases, respectively, at a phase difference of $\delta\phi = \pi/2$. In contrast to the two-node case, there are enhancements in the top-layer current and a reduction in the bottom-layer current, underscoring the significance of grounding in this case.

Fig. 7 depicts the variation of top and bottom surface Josephson currents, along with the net Josephson current, as functions of the superconducting phase difference.

Fig. 7(a) exhibits the surface currents (after subtracting this persistent flow from $J_j(\delta\phi)$), and Fig. 7(b) illustrates the net Josephson current as a function of the superconducting phase difference $\delta\phi = \phi^L - \phi^R$, respectively. In both the not-grounded and grounded cases, there exists a net current flow along the \hat{x}_{\parallel} direction. Notably, the predominant contributions to the net Josephson current originate from the top and bottom surfaces. However, in the grounded case, we observe a significant reduction in the magnitudes of the net and layer currents compared to the not-grounded case.

Fig. 7(c) and 7(d) depict the surface and net Josephson currents for the 4-node Weyl semimetal as functions of the superconducting phase difference. In the non-grounded scenario, analogous to the 2-node case, the principal contribution to the net current arises from the top and bottom surfaces. In the grounded configuration, the top surface current intensifies while the bottom surface current diminishes, resulting in a total current of comparable magnitude to the non-grounded case. This is in contrast to the 2-node case, where grounding suppresses the net current.

In the 2-node case, the Josephson current is facilitated through the occurrence of OFAR-processes, involving both surfaces. The introduction of the grounding lead induces decoherence in the system, leading to the suppression of the net current. Conversely, in the 4-node Weyl semimetal, in addition to OFAR processes, TFAR-processes occur due to the presence of the second Fermi arc. Given that TFAR processes involve both Fermi arcs and only the top surface, grounding affects OFAR processes involving the bottom surface but favors TFAR processes. This results in an increase in the top-layer current, a decrease in the bottom-layer current, and the maintenance of the net current magnitude for the 4-node Weyl semimetal case.

In the insets of Fig. 7(b) and Fig. 7(d), contributions from different j -layers in grounded and not-grounded cases for 2-node and 4-node WSMs are presented, highlighting minimal bulk current contributions.

Effect of orbital magnetic fields

Fig. 8(a) and Fig. 8(b) present the dependence of the net Josephson current (for a fixed phase difference $\delta\phi = \pi/2$) on the orbital magnetic field B_W^{orb} for the 2-node and 4-node Weyl semimetals, respectively. In the 2-node case, as depicted in Fig. 8(a), the net Josephson current exhibits an oscillatory dependence on Φ (in units of $1/\Phi_0$), where $\Phi = B_W^{\text{orb}} \times \text{Area} = L_{\parallel} L_{\perp} a_0^2$ is the area of the slab, and $\Phi_0 = \frac{h}{2e}$ is the superconducting flux quantum (in units of $\hbar = 1$ and $e = 1$).

We observe that whenever $\Phi = n\Phi_0$, where n is an integer, there is a peak in the net Josephson current. Additionally, we observe a substantial difference in the peak heights of the net Josephson current at even and odd values of n . Also, we find that grounding the bottom surface in the 2-node case suppresses the amplitude of the net Josephson current while preserving the oscillatory behavior.

Similar oscillations have also been observed in the 4-node case, as illustrated in Fig. 8(b), but with a less clear oscillation period. Additionally, in contrast to the 2-node case, grounding the bottom surfaces in this case results in the complete disappearance of these oscillations.

Our numerical results align with similar findings in theoretical works [39–42] and experimental works [43–45] and can be elucidated as follows. In the context of a surface Josephson junction, when an applied magnetic field is present along the x_{\perp} -direction, the phase difference accumulates an additional phase shift along different x_{\perp} -layers due to the applied magnetic field, given by $\frac{2\pi B_W x_{\perp} L_{\parallel}}{\Phi_0}$, where $\Phi_0 = \frac{h}{2e}$ is the superconductive flux quantum, with h being the Planck constant, and $2e$ representing the Cooper pair charge. In the current-phase relation expressions, we observed that the maximum current flow is along the edges of the top (bottom) layers of the Weyl semimetal (WSM). This allows us to express $J_c(x_{\perp}) \approx (J_c^{\text{bot.}} \delta_{x_{\perp}, 1} + J_c^{\text{top.}} \delta_{x_{\perp}, N_{\perp}})$, leading to the summed current in the form of: $J_c = (J_c^{\text{top.}} + J_c^{\text{bot.}}) \cos \left[\frac{\pi\Phi}{\Phi_0} \right]$.

In the 2-node case, the even-odd effect and periodicity of the net Josephson current can be elucidated by considering distinct conductive paths, as illustrated in Fig. 8(c-e). The top and bottom edge helical channels are connected by the left (right) edge channels. The path shown in Fig. 8(c) presents the inherent persistent current flow due to time reversal symmetry breaking, with enclosed magnetic flux $\frac{h}{e}$. The path shown in Fig. 8(d) presents the charge flow via the OFAR process, with enclosed magnetic flux $\frac{h}{2e}$.

These two-dimensional conductive paths exist for each k_W , giving rise to the even-odd Fraunhofer-like patterns in the net Josephson current. In the grounded case, these 2D paths get obstructed by the induced decoherence in the system, and the net Josephson current amplitude gets suppressed while the oscillating nature is maintained, as shown in Fig. 8(a).

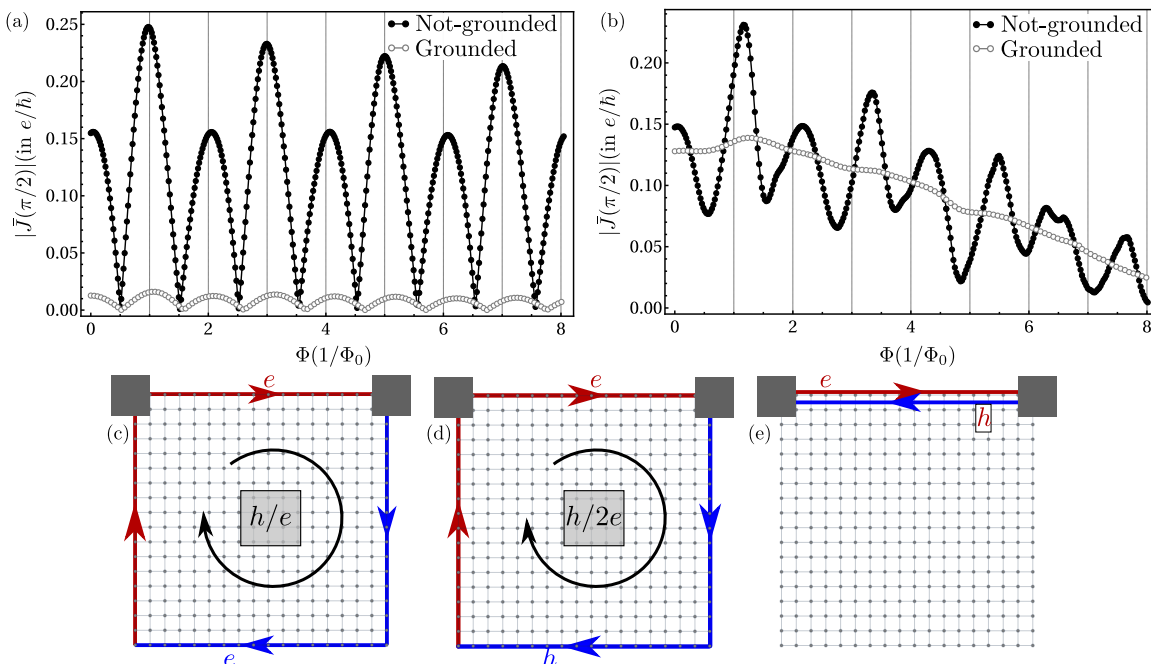


FIG. 8. Oscillations in the summed Josephson current (at a phase difference of $\pi/2$) as a function of the orbital magnetic field strength B_W for both the (a) 2-node and (b) 4-node WSM cases in a non-grounded and grounded setups. Parameters are same as Fig. 6 Conducting chiral paths for charge transfer: (c) The circulating persistent current flow of charge e . (d) OFAR process and (e) TFAR process for a $2e$ charge from the left to right reservoirs.

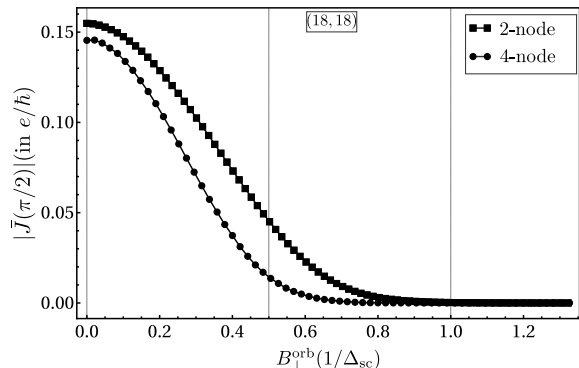


FIG. 9. Variation in the summed Josephson current as a function of applied orbital magnetic field B_{\perp}^{orb} for both the 2-node and 4-node WSM cases in the non-grounded case.

In contrast to this, in the 4-node case, an additional one-dimensional conductive path arises, as shown in Fig. 8(e), showcasing the TFAR process for $2e$ charge flow without enclosing any flux. These contributions yield a less clear oscillation period compared to the 2-node case, as this process adds up a constant contribution to the net current without enclosing any flux. Furthermore, in the grounded case, normal reservoirs obstruct the conductive paths (a-b), and only path (c) contributes to the net current, leading to the complete destruction of even-odd oscillations in the 4-node WSM, as shown in Fig. 8(b).

The variation in net Josephson current as a function of the magnetic field B_{\perp}^{orb} is shown in Fig. 9. We observe that the Josephson current decreases with an increase in

the magnetic field. This suppression in net current occurs because the magnetic field B_{\perp}^{orb} shifts the surface states to higher energy, as shown in Fig. 2(c) and Fig. 2(d), for the 2-node and 4-node WSMs, respectively.

Effect of Zeeman fields

In Fig. 10 (top row), we present the net Josephson current (for a fixed phase difference $\delta\phi = \pi/2$) as a function of applied Zeeman fields in the 2-node case. As shown in Fig. 10(a), the Zeeman field b_W serves as a controlling parameter, causing a reduction (negative values of the field) or amplification (positive values of the field) of the current. This effect results from variations in the magnetic field altering the Fermi arc length, controlling the number of edge states, and subsequently influencing the net current magnitude, as shown in Fig. 3(a).

In Fig. 10(b), we observe that the net Josephson current oscillates as a function of the Zeeman field b_{\parallel} . Additionally, the current diminishes as the applied magnetic field $|b_{\parallel}|$ increases, approaching zero for $|b_{\parallel}| \geq 2t_x$. These oscillations exhibit periodicity represented by $\theta^{2n} = \vec{k}_{2n, \parallel} L_{\parallel} \text{mod}(2\pi)$. The origin of the oscillations in net current lies in opposite momentum shifts induced by the Zeeman field in electronic and hole low-energy band dispersion. The electronic band dispersion undergoes a shift of $\vec{k}_{2n, \parallel}$, while the hole band dispersion undergoes a shift of $-\vec{k}_{2n, \parallel}$, as shown in Fig. 4(c) and Fig. 4(d), respectively.

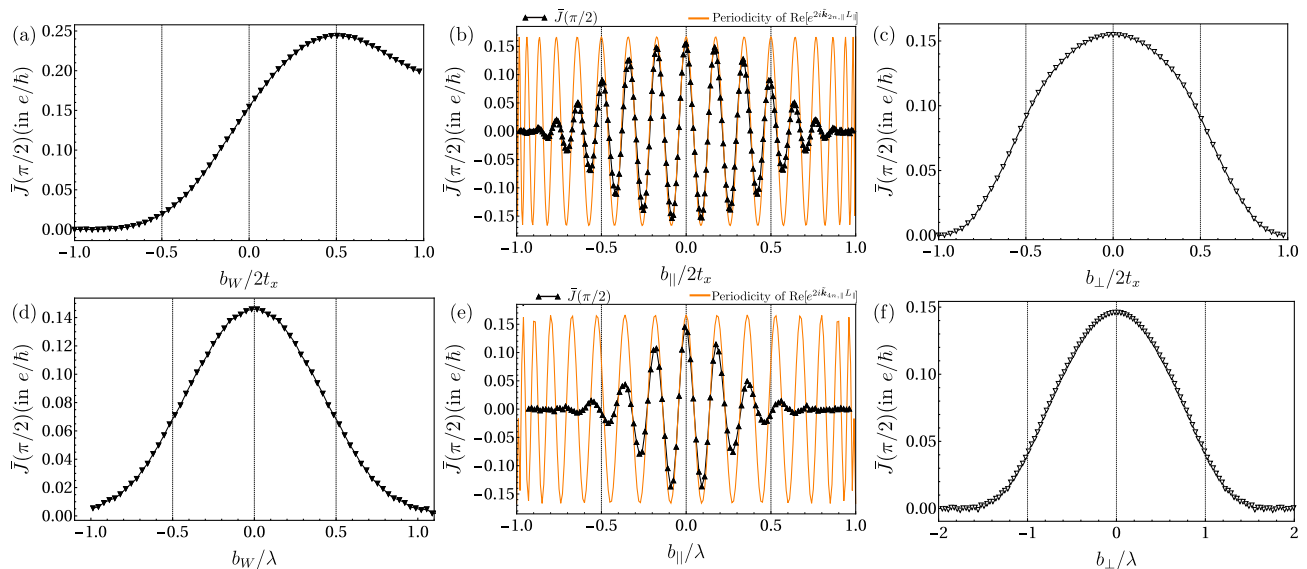


FIG. 10. Variation in summed Josephson current (at a phase difference of $\pi/2$) in the (top row) 2-node and (bottom row) 4-node WSM cases with respect to applied Zeeman fields along the b_W , b_{\parallel} , and b_{\perp} directions, in panels (a), (d); (b), (e); and (c), (f). The parameters used in these plots are identical to those in Fig. 1 and Fig. 7. Parameters M_{2n} and M_{4n} are $2t_x$ and $\sqrt{1 - m_{4n}^2}$, respectively.

In the 2-node case, the net current flow is governed by the OFAR-Andreev reflection process. When an electron traverses the top edge from the left reservoir to the right, it accumulates a phase of $e^{i\mathbf{k}_{2n,\parallel}L_{\parallel}}$, and a hole reflects from the right reservoir to the left reservoir along the bottom edge, accumulating the same phase. Consequently, a total phase accumulation of $e^{2i\mathbf{k}_{2n,\parallel}L_{\parallel}}$ occurs in this process. These accumulated phases result in distinctive oscillations in net current variation as a function of Zeeman field b_{\parallel} . In Fig. 10(b), the $\text{Im}[e^{2i\mathbf{k}_{2n,\parallel}L_{\parallel}}]$ function is also plotted to showcase the identical oscillation period between the current and the periodicity of this function.

The decrement in net Josephson current, as shown in Fig. 10(b) and Fig. 10(c), arises when the Zeeman field is oriented along the b_{\parallel} and b_{\perp} directions, respectively. These fields reduce the length of Fermi arcs, and the number of conductive edge channels decreases, proportional to the Zeeman field strength as shown in Fig. 4(a). This results in a gradual decrease and eventual zeroing of the current when the Zeeman field strength equals $2t_x$.

In Fig. 10 (bottom row), we present the net Josephson current as functions of applied Zeeman fields for the 4-node case. In contrast to the 2-node case, as shown in Fig. 10(d), the net Josephson current vanishes as a function of the Zeeman field $|b_W|$. This reduction in the current occurs because, in the 4-node case, the relative difference in the length of Fermi arcs increases in the presence of the applied Zeeman field b_W . This leads to the suppression of the TFAR process, resulting in a decrement in the net Josephson current amplitude.

In Fig. 10(e), we observe that similar to the 2-node case, the net Josephson current exhibits oscillations as a

function of Zeeman field b_{\parallel} in this case as well. Analogous to the OFAR processes, in the 4-node case, the TFAR processes also accumulate a total phase shift of $e^{2i\mathbf{k}_{4n,\parallel}L_{\parallel}}$, as shown in Fig. 4(c,e). These phase shifts result in oscillations in the variation of the net current as a function of the Zeeman field. The periodicity of these oscillations is given by $\theta^{4n} = 2\mathbf{k}_{4n,\parallel}L_{\parallel} \text{mod}(2\pi)$. In this case as well, the net current diminishes as the applied magnetic field $|b_{\parallel}|$ increases, approaching zero for $|b_{\parallel}| > |\lambda\sqrt{1 - m_{4n}^2}|$.

The suppression in net Josephson current, as shown in Fig. 10(e) and Fig. 10(f), arises when the Zeeman field is oriented along the b_{\parallel} and b_{\perp} directions, respectively. Similar to the 2-node case, $b_{\parallel(\perp)}$ fields decrease the Fermi arc lengths as shown in Fig. 4(b). Consequently, the net current gradually decreases and reaches zero when the Zeeman field strength equals $\lambda\sqrt{1 - m_{4n}^2}$.

Anomalous currents

Additionally, we also observe that the introduction of a Zeeman field b_{\parallel} leads to the emergence of ‘anomalous’ (computed for $\delta\phi = 0$) Josephson current, characterized by similar oscillations in both WSM cases. The variation in this anomalous current as a function of b_{\parallel} is shown in Fig. 11(b-c) for the 2-node and 4-node WSMs, computed using NEGF for system sizes (18, 18) and (18, 16). In Section B, a symmetry analysis has been presented for both the 2-node and 4-node cases. The anomalous current observed can be traced back to the inherent symmetries embedded within the system.

From Eq. (B9) and Eq. (B10) given in sec. B, we

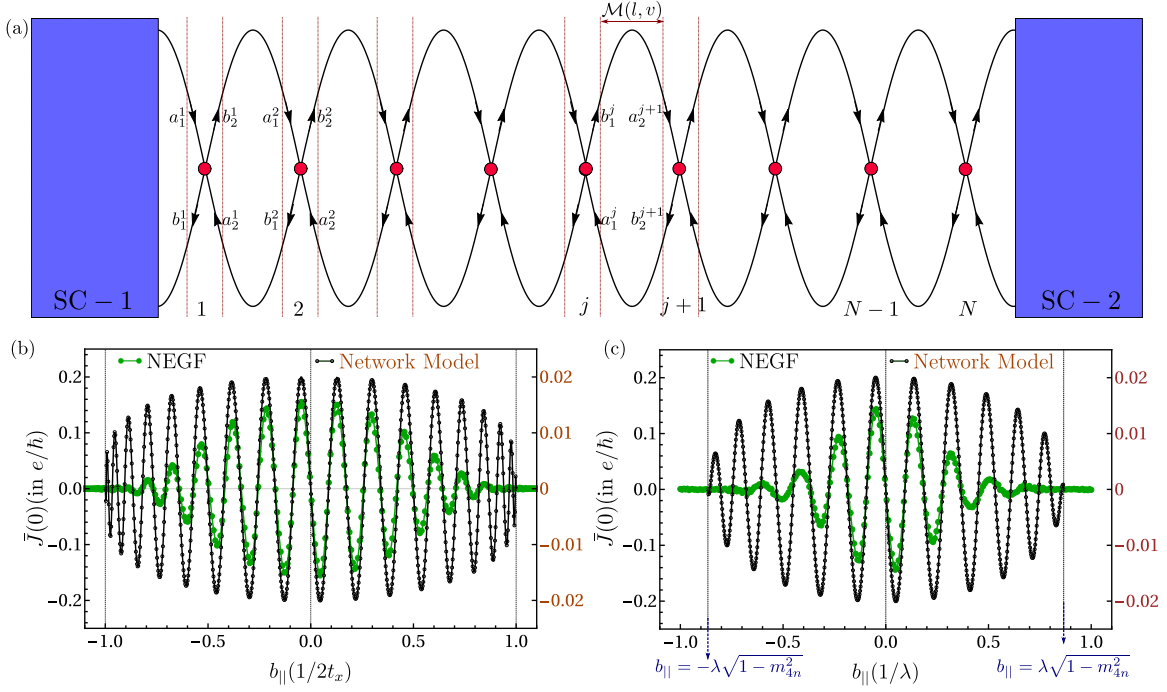


FIG. 11. Network model to study Josephson junctions: A disordered region coupled with two superconducting regions, labeled as sc1 and sc2. Variation in anomalous Josephson current (at $\delta\phi = 0$) is shown for the (a) 2-node and (b) 4-node WSM cases. The graphs display the variation in current with Zeeman fields along b_{\parallel} , reflecting $\tilde{\mathbf{k}}_{2n(4n),\parallel} L_{\parallel}$ oscillation compared to the analytically computed Josephson current, computed using a network-model study. The parameters are the same as those in Fig. 1 and Fig. 7.

observe that unique symmetry operators are identified for the 2-node and 4-node cases, represented as $\mathcal{P}_{2n} = \tilde{T}_{2n} \tilde{\sigma}_y \tilde{\mathcal{R}}_{\perp}$ and $\mathcal{P}_{4n} = \tilde{T}_{4n} |_{k_W \rightarrow -k_W} \tilde{s}_z \tilde{\sigma}_x \tilde{\mathcal{R}}_{\perp}$, respectively. This symmetry yields $\mathcal{P}_{\beta} \mathbb{H}_{\text{full}}^{\beta}(\Phi^L, \Phi^R) \mathcal{P}_{\beta}^{-1} = \mathbb{H}_{\text{full}}^{\beta}(-\Phi^L, -\Phi^R)$, where $\mathbb{H}_{\text{full}}^{\beta}$ denotes the full Hamiltonian of the Josephson junction (i.e. WSM slab connected with the superconducting reservoirs). Consequently, this symmetry implies $E(\phi) = E(-\phi)$, ensuring $I(\phi) = -I(-\phi)$ and thereby establishing the absence of anomalous current.

In the presence of the Zeeman field b_{\parallel} , this symmetry is disrupted, resulting in the emergence of anomalous current in both WSM cases, while for all other cases, this symmetry remains intact. The breakdown of this symmetry gives rise to $E_n(\phi^L, \phi^R) \neq E_n(-\phi^L, -\phi^R)$, leading to $I(\phi) \neq -I(-\phi)$ and consequently causing the presence of anomalous current. In order to gain a further understanding of this anomalous current and its oscillatory behavior, we conducted a network model study, as given in the following.

Network-model Analysis

In this section, we explain results of anomalous Josephson response in presence of b_{\parallel} field using a network model. This approach employs a network representation, as discussed in Refs. [46–48] of the Fermi arcs. Fig. 11(a) il-

lustrates the network model for a Josephson junction, where two s-wave superconductors are coupled with a chain of 1D scatterers. These scatterers are labeled $\{1, 2, \dots, j, j+1, \dots, N-1, N\}$ and function as nodes, as shown in the figure.

For this system, the Josephson current can be computed by utilizing the scattering matrix of the system. The scattering matrix of this system is constructed by directly combining the scattering matrices of individual nodes and bonds, denoted as \mathbf{s}_{node} and \mathbf{s}_{bond} , respectively. The node matrix, denoted as \mathbf{s}_{node} , has a block-diagonal structure with scattering matrices \mathbf{s}_i of individual nodes having indices $i = 1, 2, \dots$ along the diagonal. Due to electron-hole decoupling in the normal region, each \mathbf{s}_i follows a block-diagonal pattern comprising electron and hole blocks: $\mathbf{s}_{i,e}(\omega)$ and $\mathbf{s}_{i,h}(\omega) = (\mathbf{s}_{i,e}(\omega))^*$. This results in $\mathbf{s}_{\text{node}} = \mathbf{s}_{1,e}(\omega) \oplus \mathbf{s}_{1,h}(\omega) \oplus \mathbf{s}_{2,e}(\omega) \oplus \mathbf{s}_{2,h}(\omega) \oplus \dots$. In the 4-node case, these blocks also account for spin and orbital degrees of freedom, given as σ and s , respectively. In the 2-node case, these blocks only account the spin degree of freedom. The node matrices, denoted as \mathbf{s}_{node} , for each node- j has a $2m \times 2m$ (here m denotes the local degree of freedom at each site), electronic scattering matrix \mathbf{s}_j , which relates incoming and outgoing wave amplitudes of the channels, according to $\mathbf{b}^{j+1} = \mathbf{s}_j \mathbf{a}^j$, here $\mathbf{b}^j = (b_1^j, b_2^j)^T$ and $\mathbf{a}^j = (a_1^j, a_2^j)^T$. To compute the Josephson current in this system we have considered a generalized form of scattering system given

as:

$$\mathbf{s}_j = \begin{pmatrix} \cos \theta & \sin \theta \\ -\sin \theta & \cos \theta \end{pmatrix} \otimes s_0 \otimes \tau_0 \otimes \sigma_0 \quad (9)$$

The bond matrix, represented as $\mathbf{s}_{\text{bond}} = \mathcal{M}(l, v)$, incorporates phase factors for outgoing-to-incoming mode mapping, i.e. $\mathbf{a}_1^{j+1} = e^{i\epsilon l/\hbar v} \mathcal{I}_{m \times m} \mathbf{b}_2^j$ and $\mathbf{a}_2^j = e^{i\epsilon l/\hbar v} \mathcal{I}_{m \times m} \mathbf{b}_1^{j+1}$ in the scattering region. At the interface, the bond matrix contains the Andreev reflections probabilities given as: $\mathbf{a}_1^\lambda = \mathcal{M}_A(\phi^\lambda) \mathbf{b}_\lambda$, here $\mathcal{M}_A(\phi^\lambda)$ is the Andreev reflection matrix; given as $\mathcal{M}_A(\phi^\lambda)_{s'\eta'\sigma',s\eta\sigma} = i\eta'\alpha(\omega)e^{i\eta'\phi^\lambda} \delta_{s',s} \delta_{\tau',\bar{\tau}} \delta_{\sigma',\bar{\sigma}}$. Here, $\alpha(\omega) = i(\omega/\Delta_0) + \sqrt{1 - (\omega/\Delta)^2}$ and $\lambda = L, R$ represents the left, right superconducting reservoirs, respectively.

ϕ^λ is the superconducting phase of λ -t h reservoir. Indices $(s, s') \in (1, 2)$, $(\eta, \eta') \in (+1, -1)$ and $(\sigma, \sigma') \in (\uparrow, \downarrow)$ corresponds to orbital, particle-hole and spin degree of indices, respectively. For $|\omega| < \Delta$, the bond matrix $\mathbf{s}_{\text{bond}}(\omega)$ is unitary, but for $|\omega| > \Delta$, the Andreev reflection probability $|\alpha(\omega)|^2$ drops below unity due to propagating modes in the superconductor.

As derived in Ref. [47, 48], the Josephson current at temperature θ is then a sum of the logarithmic determinant over Fermionic Matsubara frequencies $\omega_p = (2p+1)k_B\theta$ (k_B is the Boltzmann constant):

$$J_0 = -\frac{k_B\theta}{2e\hbar} \sum_{p=0}^{\infty} \ln \det[1 - s_{\text{node}}(i\omega_p) \mathbf{s}_{\text{bond}}(i\omega_p)], \quad (10)$$

$$= \frac{k_B\theta}{2e\hbar} \sum_{p=0}^{\infty} \text{Tr} [1 - s_{\text{node}}(i\omega_p) \mathbf{s}_{\text{bond}}(i\omega_p)]^{-1} s_{\text{node}} \left. ds'_{\text{bond}} \right|_{i\omega_p}. \quad (11)$$

From the above-mentioned formalism, we have computed the Josephson current in this 1D Josephson junction, by probing the band-dispersion of WSM in presence of applied Zeeman field. In the presence of an applied Zeeman field, the low-energy dispersion of a WSM (energies denoted by ϵ) undergoes a shift based on the strength of the Zeeman field. As illustrated in Fig. 4, for both the 2-node and 4-node cases, the energy of the low-energy electronic and hole states shift along the momentum axis in opposite direction. This is incorporated as an additional shift in the \mathcal{M} matrices, where electronic and hole parts acquire the same phases of $\exp(i \sin^{-1}(b_{\parallel}/\gamma)l)$, where $\gamma = 2t$ and $\gamma = \lambda$ for 2 and 4-node case, respectively (see Eq. (5) and Eq. (6)). This phase difference gives rise to anomalous current and the oscillation in the Josephson currents.

Additionally, the Zeeman fields displaces the Weyl nodes and reduces the Fermi arc lengths, as depicted in

Fig. 4. Thus, we take this effect into account by multiplying the Josephson current with the length of Fermi-arc for each value of the field b_{\parallel} .

The variation in Josephson current computed using this network model study, as a function of applied Zeeman field b_{\parallel} are also presented in Fig. 11(a) and Fig. 11(b) for an identical junction length $L_{\parallel} = 18$ and $k_B\theta = 0.1$, in the 2-node and 4-node cases, respectively. Remarkably, our numerical results consistently align with the network model results.

III. CONCLUSION

In summary, this work emphasizes the importance of surface transport in Weyl Semimetals across various geometrical and electronic configurations. Specifically, we highlight the significance of one and two Fermi-arc reflection processes in surface Josephson current transport. The grounded configuration of WSM serves as a tool to differentiate between one and two Fermi-arc WSMs. Additionally, we demonstrate the impact of orbital magnetic fields on surface Josephson transport, leading to distinct even-odd Fraunhofer oscillations in the net Josephson current based on Fermi arc parity. This property can effectively distinguish between two types of Weyl semimetals in the grounded setups.

Furthermore, we explore the effects of Zeeman fields on transport, acting as parameters to measure and create the gap (by controlling the Fermi arc lengths) and tuning the Weyl node separations. Experimental setups, similar to those in Ref. [29, 49], can reveal surface transport through various voltage outcomes. Periodic anomalous oscillations of the Josephson current can be probed through Andreev spectroscopy, with the length scales of such variations typically spanning a few tens of nanometers in typical samples. Tuning Weyl node separation in momentum space is achievable by adjusting the Zeeman field [50]. These experimental configurations hold promise for generating controlled, periodically manipulable outputs through the application and adjustment of WSM nodes using Zeeman fields.

IV. ACKNOWLEDGMENTS

R. K. acknowledges the use of PARAM Sanganak and HPC 2013, facility at IIT Kanpur. The support and resources provided by PARAM Sanganak under the National Super-computing Mission, Government of India, at the Indian Institute of Technology, Kanpur, are gratefully acknowledged.

[1] B. Q. Lv, H. M. Weng, B. B. Fu, X. P. Wang, H. Miao, J. Ma, P. Richard, X. C. Huang, L. X. Zhao, G. F. Chen,

Z. Fang, X. Dai, T. Qian, and H. Ding, Experimental

- discovery of weyl semimetal taas, *Phys. Rev. X* **5**, 031013 (2015).
- [2] B. Lv, N. Xu, H. Weng, J. Ma, P. Richard, X. Huang, L. Zhao, G. Chen, C. Matt, F. Bisti, *et al.*, Observation of weyl nodes in taas, *Nature Physics* **11**, 724 (2015).
- [3] L. Yang, Z. Liu, Y. Sun, H. Peng, H. Yang, T. Zhang, B. Zhou, Y. Zhang, Y. Guo, M. Rahn, *et al.*, Weyl semimetal phase in the non-centrosymmetric compound taas, *Nature physics* **11**, 728 (2015).
- [4] H. Weng, C. Fang, Z. Fang, B. A. Bernevig, and X. Dai, Weyl semimetal phase in noncentrosymmetric transition-metal monophosphides, *Phys. Rev. X* **5**, 011029 (2015).
- [5] N. Xu, H. Weng, B. Lv, C. E. Matt, J. Park, F. Bisti, V. N. Strocov, D. Gawryluk, E. Pomjakushina, K. Conder, *et al.*, Observation of weyl nodes and fermi arcs in tantalum phosphide, *Nature communications* **7**, 11006 (2016).
- [6] Y. Tanaka, Z. Ren, T. Sato, K. Nakayama, S. Souma, T. Takahashi, K. Segawa, and Y. Ando, Experimental realization of a topological crystalline insulator in snte, *Nature Physics* **8**, 800 (2012).
- [7] B. Lv, Z.-L. Feng, Q.-N. Xu, X. Gao, J.-Z. Ma, L.-Y. Kong, P. Richard, Y.-B. Huang, V. Strocov, C. Fang, *et al.*, Observation of three-component fermions in the topological semimetal molybdenum phosphide, *Nature* **546**, 627 (2017).
- [8] H. B. Nielsen and M. Ninomiya, Absence of neutrinos on a lattice:(ii). intuitive topological proof, *Nuclear Physics B* **193**, 173 (1981).
- [9] H. B. Nielsen and M. Ninomiya, Absence of neutrinos on a lattice:(i). proof by homotopy theory, *Nuclear Physics B* **185**, 20 (1981).
- [10] M. Z. Hasan and J. E. Moore, Three-dimensional topological insulators, *Annu. Rev. Condens. Matter Phys.* **2**, 55 (2011).
- [11] A. Burkov, Topological semimetals, *Nature materials* **15**, 1145 (2016).
- [12] S. Jia, S.-Y. Xu, and M. Z. Hasan, Weyl semimetals, fermi arcs and chiral anomalies, *Nature materials* **15**, 1140 (2016).
- [13] S.-M. Huang, S.-Y. Xu, I. Belopolski, C.-C. Lee, G. Chang, B. Wang, N. Alidoust, G. Bian, M. Neupane, C. Zhang, *et al.*, A weyl fermion semimetal with surface fermi arcs in the transition metal mononictide taas class, *Nature communications* **6**, 7373 (2015).
- [14] S.-Y. Xu, N. Alidoust, I. Belopolski, Z. Yuan, G. Bian, T.-R. Chang, H. Zheng, V. N. Strocov, D. S. Sanchez, G. Chang, *et al.*, Discovery of a weyl fermion state with fermi arcs in niobium arsenide, *Nature Physics* **11**, 748 (2015).
- [15] S.-Y. Xu, I. Belopolski, N. Alidoust, M. Neupane, G. Bian, C. Zhang, R. Sankar, G. Chang, Z. Yuan, C.-C. Lee, *et al.*, Discovery of a weyl fermion semimetal and topological fermi arcs, *Science* **349**, 613 (2015).
- [16] X.-L. Qi and S.-C. Zhang, The quantum spin hall effect and topological insulators, *Physics Today* **63**, 33 (2010).
- [17] M. Zahid Hasan, S.-Y. Xu, and M. Neupane, Topological insulators, topological dirac semimetals, topological crystalline insulators, and topological kondo insulators, *Topological insulators: Fundamentals and perspectives*, 55 (2015).
- [18] P. J. Moll, N. L. Nair, T. Helm, A. C. Potter, I. Kimchi, A. Vishwanath, and J. G. Analytis, Transport evidence for fermi-arc-mediated chirality transfer in the dirac semimetal cd3as2, *Nature* **535**, 266 (2016).
- [19] S. Wang, B.-C. Lin, A.-Q. Wang, D.-P. Yu, and Z.-M. Liao, Quantum transport in dirac and weyl semimetals: a review, *Advances in Physics: X* **2**, 518 (2017).
- [20] G. Resta, S.-T. Pi, X. Wan, and S. Y. Savrasov, High surface conductivity of fermi-arc electrons in weyl semimetals, *Phys. Rev. B* **97**, 085142 (2018).
- [21] Y. Zheng, W. Chen, and D. Y. Xing, Andreev reflection in fermi-arc surface states of weyl semimetals, *Phys. Rev. B* **104**, 075420 (2021).
- [22] S. Uchida, T. Habe, and Y. Asano, Andreev reflection in weyl semimetals, *Journal of the Physical Society of Japan* **83**, 064711 (2014).
- [23] O. Vafeek and A. Vishwanath, Dirac fermions in solids: From high-*t_c* cuprates and graphene to topological insulators and weyl semimetals, *Annual Review of Condensed Matter Physics* **5**, 83–112 (2014).
- [24] W. Witczak-Krempa and Y. B. Kim, Topological and magnetic phases of interacting electrons in the pyrochlore iridates, *Phys. Rev. B* **85**, 045124 (2012).
- [25] P. Hosur, S. A. Parameswaran, and A. Vishwanath, Charge transport in weyl semimetals, *Phys. Rev. Lett.* **108**, 046602 (2012).
- [26] S. L. Adler, Axial-vector vertex in spinor electrodynamics, *Phys. Rev.* **177**, 2426 (1969).
- [27] P. E. C. Ashby and J. P. Carbotte, Chiral anomaly and optical absorption in weyl semimetals, *Phys. Rev. B* **89**, 245121 (2014).
- [28] P.-H. Fu, J. Wang, J.-F. Liu, and R.-Q. Wang, Josephson signatures of weyl node creation and annihilation in irradiated dirac semimetals, *Phys. Rev. B* **100**, 115414 (2019).
- [29] J. H. Lee, G.-H. Lee, J. Park, J. Lee, S.-G. Nam, Y.-S. Shin, J. S. Kim, and H.-J. Lee, Local and nonlocal fraunhofer-like pattern from an edge-stepped topological surface josephson current distribution, *Nano letters* **14**, 5029 (2014).
- [30] C. Li, J. C. de Boer, B. de Ronde, S. V. Ramankutty, E. van Heumen, Y. Huang, A. de Visser, A. A. Golubov, M. S. Golden, and A. Brinkman, 4π -periodic andreev bound states in a dirac semimetal, *Nature materials* **17**, 875 (2018).
- [31] C. Li, B. de Ronde, J. de Boer, J. Ridderbos, F. Zwanenburg, Y. Huang, A. Golubov, and A. Brinkman, Zeeman-effect-induced $0-\pi$ transitions in ballistic dirac semimetal josephson junctions, *Phys. Rev. Lett.* **123**, 026802 (2019).
- [32] S. Uddin, W. Duan, J. Wang, Z. Ma, and J.-F. Liu, Chiral anomaly induced oscillations in the josephson current in weyl semimetals, *Phys. Rev. B* **99**, 045426 (2019).
- [33] U. Khanna, D. K. Mukherjee, A. Kundu, and S. Rao, Chiral nodes and oscillations in the josephson current in weyl semimetals, *Phys. Rev. B* **93**, 121409(R) (2016).
- [34] U. Khanna, S. Rao, and A. Kundu, $0-\pi$ transitions in a josephson junction of an irradiated weyl semimetal, *Phys. Rev. B* **95**, 201115(R) (2017).
- [35] C.-Z. Li, A.-Q. Wang, C. Li, W.-Z. Zheng, A. Brinkman, D.-P. Yu, and Z.-M. Liao, Fermi-arc supercurrent oscillations in dirac semimetal josephson junctions, *Nature communications* **11**, 1150 (2020).
- [36] Y. Zhang, D. Bulmash, P. Hosur, A. C. Potter, and A. Vishwanath, Quantum oscillations from generic surface fermi arcs and bulk chiral modes in weyl semimetals, *Scientific reports* **6**, 23741 (2016).

- [37] T. M. McCormick, I. Kimchi, and N. Trivedi, Minimal models for topological weyl semimetals, *Physical Review B* **95**, 075133 (2017).
- [38] A. Chen and M. Franz, Superconducting proximity effect and majorana flat bands at the surface of a weyl semimetal, *Physical Review B* **93**, 201105(R) (2016).
- [39] B. Baxevanis, V. P. Ostroukh, and C. W. J. Beenakker, Even-odd flux quanta effect in the fraunhofer oscillations of an edge-channel josephson junction, *Phys. Rev. B* **91**, 041409(R) (2015).
- [40] G. Tkachov, P. Burset, B. Trauzettel, and E. M. Hankiewicz, Quantum interference of edge supercurrents in a two-dimensional topological insulator, *Phys. Rev. B* **92**, 045408 (2015).
- [41] H. Meier, V. I. Fal'ko, and L. I. Glazman, Edge effects in the magnetic interference pattern of a ballistic sns junction, *Phys. Rev. B* **93**, 184506 (2016).
- [42] Z.-T. Sun, J.-X. Hu, Y.-M. Xie, and K. T. Law, Crossover of h/e and $h/2e$ oscillations in chiral edge-channel josephson junctions, arXiv preprint arXiv:2308.01079 (2023).
- [43] V. S. Pribiag, A. J. Beukman, F. Qu, M. C. Cassidy, C. Charpentier, W. Wegscheider, and L. P. Kouwenhoven, Edge-mode superconductivity in a two-dimensional topological insulator, *Nature nanotechnology* **10**, 593 (2015).
- [44] F. K. de Vries, T. Timmerman, V. P. Ostroukh, J. van Veen, A. J. A. Beukman, F. Qu, M. Wimmer, B.-M. Nguyen, A. A. Kiselev, W. Yi, M. Sokolich, M. J. Manfra, C. M. Marcus, and L. P. Kouwenhoven, h/e superconducting quantum interference through trivial edge states in inas, *Phys. Rev. Lett.* **120**, 047702 (2018).
- [45] W. Wang, S. Kim, M. Liu, F. Cevallos, R. Cava, and N. Ong, Evidence for an edge supercurrent in the weyl superconductor mote2, *Science* **368**, 534 (2020).
- [46] D. Giuliano and I. Affleck, The josephson current through a long quantum wire, *Journal of Statistical Mechanics: Theory and Experiment* **2013**, P02034 (2013).
- [47] P. Brouwer and C. Beenakker, Anomalous temperature dependence of the supercurrent through a chaotic josephson junction, *Chaos, Solitons & Fractals* **8**, 1249 (1997).
- [48] C. W. J. Beenakker, Universal limit of critical-current fluctuations in mesoscopic josephson junctions, *Phys. Rev. Lett.* **67**, 3836 (1991).
- [49] I. Sochnikov, L. Maier, C. A. Watson, J. R. Kirtley, C. Gould, G. Tkachov, E. M. Hankiewicz, C. Brüne, H. Buhmann, L. W. Molenkamp, and K. A. Moler, Non-sinusoidal current-phase relationship in josephson junctions from the 3d topological insulator hgte, *Phys. Rev. Lett.* **114**, 066801 (2015).
- [50] B. Guo, W. Miao, V. Huang, A. C. Lygo, X. Dai, and S. Stemmer, Zeeman field-induced two-dimensional weyl semimetal phase in cadmium arsenide, *Phys. Rev. Lett.* **131**, 046601 (2023).
- [51] A. Martín-Rodero, F. J. García-Vidal, and A. Levy Yeyati, Microscopic theory of josephson mesoscopic constrictions, *Phys. Rev. Lett.* **72**, 554 (1994).

Appendix A: NUMERICAL Details

To construct the Josephson junction on the surface of the Weyl semimetal slab, we employ superconducting leads characterized by the Bogoliubov-de Gennes (BdG) Hamiltonian for a one-dimensional s -wave superconductor in the particle-hole basis. The BdG Hamiltonian ($\mathbb{H}_{\text{sc}}^\alpha$) for a superconducting lead (α) is written as:

$$\mathbb{H}_{\text{sc}}^\alpha = \frac{1}{2} \sum_{i=1}^{N_{\text{sc}}} \Phi_i^{\alpha\dagger} \left[\mu_{\text{sc}} \tau_z \sigma_0 \Phi_i^\alpha + \Delta_{\text{sc}} \sigma_0 (\tau_x \cos \phi^\alpha - \tau_y \sin \phi^\alpha) + t_{\text{sc}} \tau_z \sigma_0 \Phi_{i\pm 1}^\alpha \right]. \quad (\text{A1})$$

Here τ_z , τ_x , and τ_y are Pauli matrices acting in the particle-hole space. $\alpha = L$ and R represents the left and right superconducting reservoirs, respectively. The Nambu spinor $\Phi_i^{\alpha\dagger}$ is defined as $(c_\uparrow^\dagger, c_\downarrow^\dagger, c_\uparrow^\alpha, -c_\downarrow^\alpha)_i$, where $c_{\uparrow,i}^\dagger$ represents the creation operator for an electronic state at site i with spin \uparrow in the α -th superconductor. The superconducting phase of the α -superconductor is denoted by ϕ^α . The terms Δ_{sc} , μ_{sc} , and t_{sc} represent

the s -wave pairing gap, chemical potential, and nearest-neighbor hopping amplitude in the superconductor, respectively. N_{sc} signifies the total number of sites in each superconducting reservoir.

To construct the grounded setup, we consider normal reservoirs modeled by the Bogoliubov-de Gennes Hamiltonian for a one-dimensional normal metal in the particle-hole basis, expressed as follows:

$$\mathbb{H}_{\text{nm}}^{\bar{\alpha}} = \frac{1}{2} \sum_{i'=1}^{N_{\text{nm}}} \Phi_{i'}^{\bar{\alpha}\dagger} \left[\mu_{\text{nm}} \tau_z \sigma_0 \Phi_{i'}^{\bar{\alpha}} + t_{\text{nm}} \tau_z \sigma_0 \Phi_{i'\pm 1}^{\bar{\alpha}} \right]. \quad (\text{A2})$$

Here, $\bar{\alpha} = L$ and R represent the left and right normal reservoirs, respectively. $\Phi_{i'}^{\bar{\alpha}\dagger} = (a_\uparrow^\dagger, a_\downarrow^\dagger, a_\uparrow, -a_\downarrow)_{i'}^{\bar{\alpha}}$ and $a_{\uparrow,i}^{\bar{\alpha}}$ represents the electronic creation operator at site i and with spin \uparrow in the $\bar{\alpha}$ -th normal reservoir. μ_{nm} and t_{nm} are the chemical potential and the nearest-neighbor hopping amplitude in normal reservoir, respectively. N_{nm} represents the total number of sites in the normal reservoirs.

The tight binding Hamiltonian for the 2-node WSM slab in the BDG basis can be written as follows:

$$\mathbb{H}_{2n} = \frac{1}{2} \sum_{k_W} \sum_{i,i'=1}^{N_\parallel} \sum_{j,j'=1}^{N_\perp} \sum_{\tau\tau'\sigma\sigma'} \Psi_{ij\tau\sigma}^\dagger \tau_{\tau\tau'}^0 \sigma_{\sigma\sigma'}^x \left[(2t_x (\cos k_W - \cos k_0) + 2m_{2n}) \delta_{i,i'} \delta_{j,j'} - \left(\frac{m_{2n}}{2} \tau_{\tau\tau'}^0 \sigma_{\sigma\sigma'}^x \pm i \tau_{\tau\tau'}^z \sigma_{\sigma\sigma'}^y t \right) \delta_{i',i\pm 1} \delta_{j,j'} - \left(\frac{m_{2n}}{2} \tau_0^{\tau\tau'} \sigma_{\sigma\sigma'}^x \pm i \tau_{\tau\tau'}^z \sigma_{\sigma\sigma'}^z t \right) \delta_{i',i} \delta_{j',j\pm 1} \right] \Psi_{i'j'\tau'\sigma'}. \quad (\text{A3})$$

$$\mathbb{H}_{4n} = \frac{1}{2} \sum_{k_W} \sum_{i,i'=1}^{N_\parallel} \sum_{j,j'=1}^{N_\perp} \sum_{\sigma\tau\tau'\sigma'} \Psi_{i,j,s,\sigma}^\dagger \left[(\lambda s_{ss'}^0 \tau_{\tau\tau'}^0 \sigma_{\sigma\sigma'}^y \sin k_W + (m_{4n} + 2) s_{ss'}^y \tau_{\tau\tau'}^0 \sigma_{\sigma\sigma'}^y) \delta_{i,i'} \delta_{j,j'} - \frac{1}{2} \left(s_{ss'}^y \tau_{\tau\tau'}^0 \sigma_{\sigma\sigma'}^y \pm i \lambda s_{ss'}^0 \tau_{\tau\tau'}^z \sigma_{\sigma\sigma'}^x \right) \delta_{i',i\pm 1} \delta_{j,j'} - \frac{1}{2} \left(s_{ss'}^y \tau_{\tau\tau'}^0 \sigma_{\sigma\sigma'}^y \pm i \lambda s_{ss'}^0 \tau_{\tau\tau'}^z \sigma_{\sigma\sigma'}^x \right) \delta_{i',i\pm 1} \delta_{j',j'} \right] \Psi_{i',j',s'\sigma'}. \quad (\text{A4})$$

Here, the Nambu spinors are defined as $\Psi_{ij}^\dagger = (\psi_\uparrow^\dagger, \psi_\downarrow^\dagger, \psi_\downarrow, -\psi_\uparrow)_{ij}$ and $\Psi_{ij}^\dagger = (\psi_{1\uparrow}^\dagger, \psi_{1\downarrow}^\dagger, \psi_{2\uparrow}^\dagger, \psi_{2\downarrow}^\dagger, \psi_{1\downarrow}, -\psi_{1\uparrow}, \psi_{2\downarrow}, -\psi_{2\uparrow})_{ij}$, in equations (A3) and (A4), respectively. i and j correspond to the site indices of the slab geometry, where i is along the x_\parallel direction, and j is along the x_\perp direction. N_\parallel and N_\perp represent the number of sites in the x_\parallel and x_\perp directions, respectively.

To establish a connection between the reservoirs and the surfaces of the Weyl semimetal slab, we introduce tunneling matrix Hamiltonians as described by:

$$\mathbb{H}_T^{\beta,\alpha'} = \frac{1}{2} \Psi_r^\dagger V_{rr'}^{\beta,\alpha'} \Phi_{r'}^{\alpha'} + \text{h.c.}, \quad (\text{A5})$$

The matrix elements $V_{rr'}^{\beta,\alpha'}$ contain details about the tunneling links specific to sites identified by (r, r') . $\beta = 2n$ and $4n$ specify the coupling in the case of the 2-node and 4-node WSM, respectively. r and r' correspond to

coordinates within the WSM and the α' -th reservoir, respectively.

For the Josephson junction positioned along the top surface, the values of $\{r, r'\}$ are set to $\{(L_\perp, 1), N_{\text{sc}}\}$ and $\{(L_\perp, L_\parallel), 1\}$, indicating the connections with the left and right superconducting reservoirs, respectively. The phase of these left and right superconducting reservoirs are given by ϕ^L and ϕ^R , respectively. The superconducting phase difference is given as $\delta\phi = \phi^R - \phi^L$. For the grounded case, the values of $\{r, r'\}$ are set to $\{(1, 1), N_{\text{nm}}\}$ and $\{(1, L_\parallel), 1\}$, indicating the connections with the left and right normal reservoirs, respectively.

In the cases of the Josephson junction of the 2-node and 4-node WSM, the tunneling matrix elements are given by:

$$V_{r,r'}^{2n,\alpha'} = t_{\alpha'} \delta_{r,r'} \tau_z \sigma_0 \quad (\text{A6})$$

$$V_{r,r'}^{4n,\alpha'} = t_{\alpha'} \delta_{r,r'} \begin{pmatrix} \tau_z \sigma_0 & 0 \\ 0 & \tau_z \sigma_0 \end{pmatrix} \quad (\text{A7})$$

The Green's function of the full system (WSM slab connected with reservoirs), is defined as follows:

$$G_\beta(\omega) = \left(\omega \mathbb{I} - \mathbb{H}_\beta - \sum_{\alpha'} \Sigma_{\alpha'}^\beta(\omega) \right)^{-1}. \quad (\text{A8})$$

Here, \mathbb{H}_β is given by Eq. (A3) and Eq. (A4) in the case of the 2-node and 4-node WSM, respectively. $\Sigma_{\alpha'}^\beta(\omega) = V^{\beta,\alpha'} g^{\alpha'}(\omega) V^{\beta,\alpha'\dagger}$ is the self-energy term corresponding to the α' reservoir, where $g^{\alpha'}(\omega)$ represents the Green's functions for the α' -th reservoir.

In this system, the bond current flow at site (i, j) can be expressed as $\hat{J}_{ij}^\beta = (ie/\hbar) [\mathbb{H}_\beta, N_{ij}^\beta]$, where N_{ij}^β represents the electronic number operator at site (i, j) . For the 2-node WSM, the net current flow along the x_\parallel and x_\perp directions is given by the following expressions:

$$\begin{aligned} \langle \hat{J}_{(i \rightarrow i+1, j)}^{2n} \rangle &= -\frac{e}{\hbar} \sum_{k_W \sigma \sigma'} \left(\frac{m_{2n}}{2} \text{Im} \left[\langle \psi_{i,j,\sigma}^\dagger \psi_{i+1,j,\sigma'} \rangle \right] + t\sigma' \right. \\ &\quad \left. \text{Re} \left[\langle \psi_{i,j,\sigma}^\dagger \psi_{i+1,j,\sigma'} \rangle \right] \right), \end{aligned} \quad (\text{A9})$$

$$\langle \hat{J}_{(i, j \rightarrow j+1)}^{2n} \rangle = -\frac{e}{\hbar} \sum_{k_W \sigma \sigma'} \left(\frac{m_{2n}}{2} - t\sigma \right) \text{Im} \left[\langle \psi_{i,j,\sigma}^\dagger \psi_{i,j+1,\sigma'} \rangle \right]. \quad (\text{A10})$$

Similarly, for the 4-node WSM, the net current flow along the x_\parallel and x_\perp directions is given by the following expressions:

$$\begin{aligned} \langle \hat{J}_{(i \rightarrow i+1, j)}^{4n} \rangle &= -\frac{e}{2\hbar} \sum_{k_W \sigma \sigma'} \left(\lambda \sigma' \text{Re} \left[\langle \psi_{i,j,s,\sigma}^\dagger \psi_{i+1,j,s,\sigma'} \rangle \right] \right. \\ &\quad \left. + s\sigma' \text{Im} \left[\langle \psi_{i,j,s,\sigma}^\dagger \psi_{i+1,j,s,\sigma'} \rangle \right] \right), \end{aligned} \quad (\text{A11})$$

$$\begin{aligned} \langle \hat{J}_{(i, j \rightarrow j+1)}^{4n} \rangle &= -\frac{e}{2\hbar} \sum_{k_W \sigma \sigma'} \left(\lambda \text{Re} \left[\langle \psi_{i,j,s,\sigma}^\dagger \psi_{i,j+1,s,\sigma'} \rangle \right] \right. \\ &\quad \left. + s\sigma' \text{Im} \left[\langle \psi_{i,j,s,\sigma}^\dagger \psi_{i,j+1,s,\sigma'} \rangle \right] \right). \end{aligned} \quad (\text{A12})$$

In the above mentioned equations, $\sigma' = +1$ and -1 represent the spin-up and spin-down cases, respectively. Similarly, $s = +1$ and -1 correspond to orbital-1 and orbital-2 cases, respectively. The symbol $\langle \cdot \rangle$ signifies the thermal average taken over the states of the reservoir. The averages $\langle \cdot \rangle$ in the above equations can be computed using the Non-Equilibrium Green's Function approach [51] as:

$$G_{\beta, r' r}^{+-}(t, t') = i \begin{pmatrix} \langle \psi_r^\dagger(t) \psi_{r'}(t') \rangle & \langle \psi_r(t) \psi_{r'}(t') \rangle \\ \langle \psi_r^\dagger(t) \psi_r^\dagger(t') \rangle & \langle \psi_r(t) \psi_r^\dagger(t') \rangle \end{pmatrix} \quad (\text{A13})$$

In this equation, r and r' represent site indices encompassing the information of the corresponding local degree of freedom. Using Fourier transform, we can write:

$$G_\beta^{+-}(\omega) = f(\omega) [G_\beta^A(\omega) - G_\beta^R(\omega)]. \quad (\text{A14})$$

In the above equation, $G_\beta^A(\omega)$ and $G_\beta^R(\omega)$ refer to the advanced and retarded Green's functions, respectively.

The bond currents along distinct bonds in the x_\parallel and x_\perp directions are calculated using Eq. (A9) and Eq. (A10) in the 2-node case, and Eq. (A11) and Eq. (A12) in the 4-node case, respectively. The net Josephson current along the x_\parallel direction is obtained by summing over the index- j from 1 to N_\perp , in Eq. (A9) and Eq. (A11) for the 2-node and 4-node cases, respectively.

Appendix B: Symmetry Analysis

This section explains the presence of anomalous current using the symmetry analysis of the individual of full Hamiltonian (WSM slab connected with reservoirs) in the 2-node and 4-node cases. In the case of 2-node WSM slab, these terms can be expressed as:

$$\begin{aligned} h^{2n, M} &= (2t_x (\cos k_W - \cos k_0) + 2m_{2n}) \mathbf{I}_N \otimes \tau_0 \otimes \sigma_x \\ &\quad - \frac{m_{2n}}{2} (\mathcal{A} + \mathcal{B}) \otimes \tau_0 \otimes \sigma_x \end{aligned} \quad (\text{B1})$$

$$h^{2n, \parallel} = \pm it \mathcal{A} \otimes \tau_z \otimes \sigma_x. \quad (\text{B2})$$

$$h^{2n, \perp} = \pm it \mathcal{B} \otimes \tau_z \otimes \sigma_x. \quad (\text{B3})$$

Here, $h^{2n, M}$ represents the diagonal and off-diagonal contributions of the mass term, whereas $h^{2n, \parallel}$ and $h^{2n, \perp}$ correspond to the off-diagonal spin-orbit terms along the i (x_\parallel) and j (x_\perp) directions, respectively. Additionally, the matrices $\mathcal{A}_{(i,j), (i',j')} = \delta_{i', i \pm 1} \delta_{j, j'}$, $\mathcal{B}_{(i,j), (i',j')} = \delta_{j', j \pm 1} \delta_{i, i'}$ and \mathbf{I}_N is the identity matrix of size N . For the WSM slab N is given as $(N_\parallel \times N_\perp)$. For the superconductors:

$$\begin{aligned} h_{\text{sc}}(\delta\phi) &= \sum_{\alpha} \left[\mu_{\text{sc}} \mathbf{I}_N \otimes \tau_z \otimes \sigma_0 + \Delta_{\text{sc}} \mathbf{I}_N \otimes (\tau_x \cos \phi^\alpha - \right. \\ &\quad \left. \tau_y \sin \phi^\alpha) \otimes \sigma_0 + t_{\text{sc}} \mathcal{A} \otimes \tau_z \otimes \sigma_0 \right] \end{aligned} \quad (\text{B4})$$

In addition to this terms, $\sum_{\alpha, \beta} V_{rr'}^{\beta, \alpha}$ correspond to the tunneling terms which connects the reservoirs at the surfaces of WSM slab as defined in Eq. (A6). Furthermore, the Zeeman field terms \tilde{b}_W^{2n} , \tilde{b}_\parallel^{2n} , and \tilde{b}_\perp^{2n} in the BDG basis, are represented by $b_W \tau_0 \sigma_x$, $b_\parallel \tau_0 \sigma_y$, and $b_\perp \tau_0 \sigma_z$. Similarly, in the 4-node case,

$$h^{4n, d} = i\lambda \sin k_y \mathbf{I}_N \otimes s_0 \otimes \tau_0 \otimes \sigma_y; \quad (\text{B5})$$

$$\begin{aligned} h^{4n, M} &= (m_{4n} + 2) \mathbf{I}_N \otimes s_y \otimes \tau_0 \otimes \sigma_y - \frac{1}{2} (\mathcal{A} + \mathcal{B}) \otimes \\ &\quad s_y \otimes \tau_0 \otimes \sigma_y. \end{aligned} \quad (\text{B6})$$

$$h^{4n, \parallel} = \pm i\lambda \mathcal{A} \otimes s_0 \otimes \tau_z \otimes \sigma_x. \quad (\text{B7})$$

$$h^{4n, \perp} = \pm i\lambda \mathcal{B} \otimes s_0 \otimes \tau_z \otimes \sigma_x. \quad (\text{B8})$$

Here, $h^{4n, d}$ and $h^{4n, M}$ represents the diagonal and off-diagonal contributions of the mass term, whereas $h^{4n, \parallel}$ and $h^{4n, \perp}$ correspond to the off-diagonal spin-orbit terms along the i (x_\parallel) and j (x_\perp) directions, respectively.

Additionally, the matrices. In addition to this terms, $\sum_{\alpha,\beta} V_{rr'}^{\beta,\alpha}$ correspond to the tunneling terms which connects the reservoirs at the surfaces of WSM slab as defined in Eq. (A7). Furthermore, the Zeeman field terms \tilde{b}_W^{4n} , $\tilde{b}_{\parallel}^{4n}$, and \tilde{b}_{\perp}^{4n} in the BDG basis, are represented by $b_W s_0 \otimes \tau_0 \otimes \sigma_y$, $b_{\parallel} s_0 \otimes \tau_0 \otimes \sigma_x$, and $b_{\perp} s_0 \otimes \tau_0 \otimes \sigma_z$.

The symmetries of these individual terms in the in the case of 2-node WSM can be expressed as:

$$\begin{array}{c} \left[\begin{array}{cccccccc} \cdot & h^{2n,M} & h^{2n,\parallel} & h^{2n,\perp} & \tilde{b}_W^{2n} & \tilde{b}_{\parallel}^{2n} & \tilde{b}_{\perp}^{2n} & h_{\text{sc}}(\delta\phi) \\ \tilde{\mathcal{T}}_{2n} & - & + & + & - & - & - & \delta\phi \rightarrow -\delta\phi \\ \tilde{\sigma}_x & + & - & - & + & - & - & + \\ \tilde{\sigma}_y & - & + & - & - & + & - & + \\ \tilde{\sigma}_z & - & - & + & - & - & + & + \\ \tilde{\mathcal{R}}_{\parallel} & + & - & + & + & + & + & \delta\phi \rightarrow -\delta\phi \\ \tilde{\mathcal{R}}_{\perp} & + & + & - & + & + & + & + \end{array} \right] \end{array} \quad (\text{B9})$$

Here, the symbols ‘+’ and ‘-’ represent the signs accumulated in given terms in first row under the symmetry operators given in the corresponding entries in the first column. These symmetries include time-reversal indicated as $\tilde{\mathcal{T}}_{2n} = \mathbf{I}_N \otimes \mathcal{T}_{2n}$. Spatial inversions along \parallel and \perp -directions, denoted as $\tilde{\mathcal{R}}_{\parallel} = \mathbf{I}_N \otimes \tau_0 \otimes \sigma_0 \otimes \mathcal{R}_{\parallel}$ and $\tilde{\mathcal{R}}_{\perp} = \mathbf{I}_N \otimes \tau_0 \otimes \sigma_0 \otimes \mathcal{R}_{\perp}$. Spin rotations denoted as $\tilde{\sigma}_x = \mathbf{I}_N \otimes \tau_0 \otimes \sigma_x$, $\tilde{\sigma}_y = \mathbf{I}_N \otimes \tau_0 \otimes \sigma_y$, and $\tilde{\sigma}_z = \mathbf{I}_N \otimes \tau_0 \otimes \sigma_z$.

The symmetries of these individual terms in the in the case of 4-node WSM can be expressed as:

$$\begin{array}{c} \left[\begin{array}{cccccccc} \cdot & h^{4n,M} & h^{4n,d} & h^{2n,\parallel} & h^{2n,\perp} & \tilde{b}_{\parallel}^{4n} & \tilde{b}_W^{4n} & \tilde{b}_{\perp}^{4n} & h_{\text{sc}}(\delta\phi) \\ \tilde{\mathcal{T}}_{4n} & + & + & + & + & - & - & - & \delta\phi \rightarrow -\delta\phi \\ \tilde{\sigma}_x & - & - & + & - & + & - & - & + \\ \tilde{\sigma}_y & + & + & - & - & - & + & - & + \\ \tilde{\sigma}_z & - & - & - & + & - & - & + & + \\ \tilde{s}_x & - & + & + & + & + & + & + & + \\ \tilde{s}_y & + & + & + & + & + & + & + & + \\ \tilde{s}_z & - & + & + & + & + & + & + & + \\ \mathcal{R}_{\parallel} & + & + & - & + & + & + & + & \delta\phi \rightarrow -\delta\phi \\ \mathcal{R}_{\perp} & + & + & + & - & + & + & + & + \end{array} \right] \end{array} \quad (\text{B10})$$

Here, these symmetries include time-reversal indicated as $\tilde{\mathcal{T}}_{4n} = \mathbf{I}_N \otimes \mathcal{T}_{4n}$. Spatial inversions along \parallel and \perp -directions, denoted as $\tilde{\mathcal{R}}_{\parallel} = \mathbf{I}_N \otimes s_0 \otimes \tau_0 \otimes \sigma_0 \otimes \mathcal{R}_{\parallel}$ and $\tilde{\mathcal{R}}_{\perp} = \mathbf{I}_N \otimes s_0 \otimes \tau_0 \otimes \sigma_0 \otimes \mathcal{R}_{\perp}$. Spin rotations denoted as $\tilde{\sigma}_x = \mathbf{I}_N \otimes s_0 \otimes \tau_0 \otimes \sigma_x$, $\tilde{\sigma}_y = \mathbf{I}_N \otimes s_0 \otimes \tau_0 \otimes \sigma_y$, and $\tilde{\sigma}_z = \mathbf{I}_N \otimes s_0 \otimes \tau_0 \otimes \sigma_z$.

Using Eq. (B9) and Eq. (B10), for 2-node and 4-node cases we have defined the symmetry operators $\mathcal{P}_{2n} = \mathcal{T}_{2n} \sigma_y \mathcal{R}_{\perp}$ and $\mathcal{P}_{4n} = \mathcal{T}_{4n} |_{k_W \rightarrow -k_W} s_z \sigma_x \mathcal{R}_{\perp}$, respectively. This symmetry gives rise to $\mathcal{P}_{\beta} \mathbb{H}_{\text{full}}^{\beta}(\Phi^L, \Phi^R) \mathcal{P}_{\beta}^{-1} = \mathbb{H}_{\text{full}}^{\beta}(-\Phi^L, -\Phi^R)$, where $\mathbb{H}_{\text{full}}^{\beta}$ represents the full Hamiltonian of the Josephson junction. This implies $E(\phi) = E(-\phi)$ and ensures $I(\phi) = -I(-\phi)$, ensuring the absence of anomalous current.

When the Zeeman field b_{\parallel} is applied, we observe that this Zeeman field term disrupts this symmetry, resulting in the emergence of anomalous current in both WSM cases. This symmetry breaking leads to $E_n(\phi^L, \phi^R) \neq E_n(-\phi^L, -\phi^R)$, resulting in $I(\phi) \neq -I(-\phi)$ and causing the presence of anomalous current. To understand this anomalous current and oscillatory behavior further, we employed a network model study given in following section.